ARTICLE IN PRESS

Journal of Colloid and Interface Science xxx (xxxx) xxx

Contents lists available at ScienceDirect

Journal of Colloid and Interface Science

journal homepage: www.elsevier.com/locate/jcis

Regular Article

Surface activation towards manganese dioxide nanosheet arrays *via* plasma engineering as cathode and anode for efficient water splitting

Pengcheng Wang [a], Yaotian Yan [a], Jian Cao [b], Jicai Feng [a], Junlei Qi [a,*]

[a] State Key Laboratory of Advanced Welding and Joining, Harbin Institute of Technology, Harbin 150001, China
[b] School of Materials Science and Engineering, Harbin Institute of Technology, Harbin, China

GRAPHICAL ABSTRACT

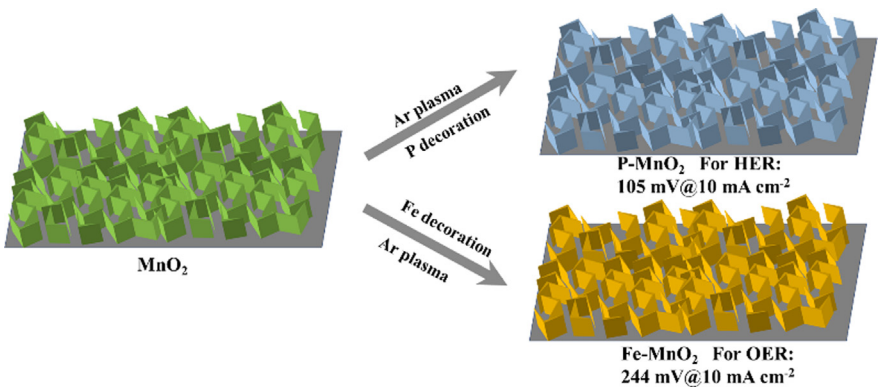

ARTICLE INFO

Article history:
Received 10 August 2020
Revised 17 October 2020
Accepted 19 October 2020
Available online xxxx

Keywords:
MnO_2
Surface activation
Active species
Vacancies
Plasma engineering

ABSTRACT

Developing high-efficiency, low-cost electrocatalysts for water splitting is important but challenging. Two-dimensional nanosheet manganese dioxide (MnO_2) arrays are promising candidates for the design and development of advanced catalysts because of their large surface area. Here, a feasible solution to improve the catalytic activity of MnO_2 materials *via* decorating the active sites on the surface is proposed. With the help of plasma engineering, we successfully enabled surface activity of the MnO_2 nanosheets by decorating P or Fe species together with rich vacancies on the surface. The decorated P (P-MnO_2) or Fe (Fe-MnO_2) species were highly beneficial for the absorption of protons and OH^- respectively, and rich oxygen vacancies induced the formation of stable Mn^{3+}, which contributed to electron and charge transfer. Thus, increased electrochemically active specific areas, accelerated charge transfer, and a proper surface electronic structure could be achieved. On the basis of this activation strategy, the fabricated P-MnO_2 and Fe-MnO_2 showed excellent catalytic performance for the hydrogen evolution and oxygen evolution reactions. To our knowledge, the performance of P-MnO_2 and Fe-MnO_2 outperformed most MnO_2-based electrocatalysts in the field of electrocatalytic water splitting. Surface activation of two-dimensional MnO_2 materials by decorating active species *via* plasma treatment can provide a feasible route for modulating the performance of earth-abundant electrocatalysts for practical applications.

* Corresponding author.
E-mail address: jlqi@hit.edu.cn (J. Qi).

https://doi.org/10.1016/j.jcis.2020.10.073
0021-9797/

1. Introduction

Electrocatalytic water splitting has been considered as a promising method to ease the energy crisis [1,2]. Hydrogen is regarded as a green and sustainable alternative to fossil fuels. Among the many hydrogen production technologies, water splitting is an effective way to produce high-purity hydrogen, and it consists of the hydrogen evolution (HER) and the oxygen evolution reactions (OER). To increase the production efficiency and save energy, effective electrocatalysts are needed to accelerate the reaction kinetics of HER and OER and reduce the overpotential [3,4]. Currently, state-of-art high-efficiency Pt and Ir/Ru-based oxides catalysts are used for HER and OER, respectively. However, the scarcity and cost of these noble metal-based catalysts greatly limit their scaled development and application [5]. Consequently, it is of great significance to explore low-cost electrocatalysts with satisfactory HER and OER efficiencies.

Recently, transition metal-based two-dimensional (2D) materials have attracted increasing attention in the field of electrocatalytic water splitting because of their large specific surface area, which ensures exposed active sites [6,7]. Among them, manganese dioxide, which contains rich edge-sharing MnO_6 octahedrites, has indicated promising potential for electrocatalytic water splitting. The oxygen vacancies and multiple valences of Mn present in the layered δ-MnO_2 could benefit the HER and OER catalytic processes [8]. Zhang et al. successfully synthesized defect-engineered δ-MnO_2 nanosheets and applied them toward overall water splitting [9]. Oxygen vacancies play a key role in inducing the formation of Mn^{3+} sites, which serve as highly active sites for promoting conductivity and H_2O adsorption. Mn^{3+} can lead to a more ideal adsorption energy for the proton intermediate species during the HER, as well as promoting OER via the disproportionation reaction. However, the limited amount of active sites still poses an important challenge for the design of high-performance electrocatalysts [10–12].

Notably, surface activation *via* decoration with electroactive species (anions and cations) on the surface has been demonstrated as an efficient method for improving the catalytic activity *via* the introduction of highly active sites [13]. Lv et al. demonstrated that P atoms usually play a significant role in promoting HER because the partial negative charges caused by the polarization of the P atoms greatly benefits the adsorption of protons [14,15]. Friebel et al. demonstrated that Fe^{3+} was beneficial for OER electrocatalysis *via* efficient adsorption of H_2O molecules and the OH^- species [16]. In view of this, 2D materials provide a large surface area for decoration with electroactive sites. Considering the modulation effects on the electronic structure caused by vacancies, the development of new strategies that combine decorated active species and vacancies is of interest.

In this work, using plasma engineering for the fabrication of MnO_2 nanosheets, we successfully constructed sheets with rich vacancies and decorated P anions for HER and Fe cations for OER. With this strategy, the decorated active species and oxygen vacancies clearly increased the active sites, adjusted the electronic structure, and accelerated electrical conductivity during the catalytic process. Our activation strategy successfully addressed the poor HER catalytic activity and improved the OER performance of the MnO_2 nanosheets. As a result, MnO_2 nanosheets with surface activation showed remarkable catalytic activities with low overpotentials of 105 mV and 244 mV for HER and OER, respectively. To the best of our knowledge, such catalytic performances outperform most MnO_2-based electrocatalysts in the field of overall water splitting. On application in a two-electrode electrolyzer, only a low voltage of 1.59 V was needed to achieve 10 mA cm^{-2}. This work focused on surface activation *via* plasma engineering to introduce decorated active species and numerous vacancies for efficient electrocatalytic water splitting.

2. Materials and method

2.1. Reagents

Chemicals: Potassium permanganate ($KMnO_4$) was purchased from Beijing Chemical works. Iron nitrate nonahydrate ($Fe(NO_3)_3 \cdot 9H_2O$, 99%) and Sodium hypophosphite monohydrate ($NaH_2PO_2 \cdot H_2O$, 99%) were purchased from Aladdin Reagent Co., Ltd. Ni foam (NF) was purchased from Hefei kejing material Technology Co., Ltd. Of Hefei, China. The Ni foam (2 cm × 5 cm) was cleaned by acetone for 10 min and aqueous HCl for 10 min, then was rinsed with water and ethanol for several times.

2.2. Synthesis of P-MnO2 and Fe-MnO 2 electrocatalysts

Fabrication of MnO_2 nanosheet array: Typically, 4 mmol potassium permanganate ($KMnO_4$) was dissolved in 80 mL deionized water to form a mixed solution after mechanical stirring. The mixed solution with treated Ni foam was transferred to 100 mL Teflon-lined stainless-steel autoclave, and heating at 180 °C for 3 h. After that, the Ni foam with MnO_2 product was collected after washing with distilled water and ethanol for several times, and then dried overnight.

Fabrication of E-MnO_2 nanosheet array: The obtained MnO_2 was placed in the tubular PECVD system (PECVD, OTF-1200X-50-4CLV-PE) under 0.5 torr and heated in the Ar flow of 10 sccm. When heated to 200 °C, the MnO_2 was treated with Ar plasma at 200 W for 10 min.

Fabrication of P-MnO_2 nanosheet arrays: The 0.3 g $NaH_2PO_2 \cdot H_2O$ and MnO_2 were put in the upstream and downstream side of the tube furnace under 0.5 torr and heated in the Ar flow of 10 sccm, respectively. When the upstream and downstream sides were heated to 300 and 200 °C, respectively. Then, the MnO_2 was treated with Ar plasma under the PH_3 atmosphere at 200 W for 1, 5, 10 and 20 min (denoted as P-MnO_2-1, 5, 10, 20), respectively. The optimal sample was marked hereafter as P-MnO_2.

Fabrication of Fe-MnO_2 nanosheet arrays: The obtained MnO_2 was immersed in $Fe(NO_3)_3 \cdot 9H_2O$/ethanol solution for 10 min, and air dried. Different amounts (0.02, 0.05, 0.1 and 0.2 g) of $Fe(NO_3)_3 \cdot 9H_2O$ were conducted to obtain various dopant of Fe element. The dried sample was placed in the tubular under 0.5 torr and heated under the Ar flow of 10 sccm. When heated to 200 °C, the dried sample was treated with Ar plasma at 200 W for 10 min to obtain Fe-MnO_2-0.02, 0.05, 0.1, 0.2. The optimal sample was shortly demoted hereafter as Fe-MnO_2.

2.3. Sample characterization

Scanning electron microscopy (SEM), Transmission electron microscopy (TEM) and X-ray diffraction (XRD) were applied to investigate the nanostructure, morphology and crystalline phases of obtained samples. X-ray photoelectron spectra (XPS) and electron paramagnetic resonance (EPR) was used to investigate the surface states. The corresponding characterization methods can refer to the literature [17–22].

2.4. Electrochemical measurements

All electrochemical performances were measured in the electrochemical workstation (CHI 760E and PARSTAT 4000A). The OER and HER properties were measured in a three-electrode system,

using obtained samples, Hg/HgO and carbon rod as working electrode and reference electrode and counter electrode, respectively. All the potential was converted to reversible hydrogen electrode (RHE). The polarization curves were collected at 2 mV s^{-1} in 1 M KOH solution, and compensated with iR-correction. And R can be obtained from an EIS Nyquist plot as the first intercept of the main arc with the real axis. Before OER and HER tests, all samples were cycled at 10 mV s^{-1} until the stability of cyclic voltammetry (CV), then the data were collected. The overall water splitting was tested in the two-electrode system. The reference electrodes of Pt/C (20 wt%) and RuO_2 were also prepared on carbon cloth, and the prepared method was according to previously reported researches [23,24].

3. Results and discussions

Scheme 1 shows the schematic fabrication of the P-MnO_2 and Fe-MnO_2 nanosheet arrays. The MnO_2 nanosheets are achieved through following process. Firstly, MnO_2 nanosheet arrays are synthesized on Ni foam by the hydrothermal process. Subsequently, P species and oxygen vacancies are concurrently decorated on the surface of MnO_2 nanosheets *via* Ar plasma for HER, besides, Fe species and oxygen vacancies are concurrently introduced on the surface *via* Ar plasma treatment for OER.

Fig. 1 shows the microstructures and crystalline phases of the optimal samples. The SEM image (Fig. 1a) clearly shows the edge-shared nanosheet morphologies in the pristine MnO_2 nanosheets with smooth surfaces that are uniformly grown on the Ni foam. The morphology of the MnO_2 nanosheets were further confirmed *via* TEM, as shown in Fig. 1b and the results correspond well with the SEM results. From the high-resolution TEM (HRTEM) image in Fig. 1c, a lattice spacing of ~0.214 nm corresponding to the (015) facet of MnO_2 was determined. The XRD spectra (Fig. 1d) show that all the diffraction peaks can correspond well with the δ-MnO_2 phase (JCPDS Card No. 86-0666).

Subsequently the pristine MnO_2 nanosheets were etched *via* plasma treatment. As shown in Fig. S1, E-MnO_2 maintained a rough and porous nanosheet structure because of the etching effect of the Ar plasma. After decorating with P or Fe species *via* plasma treatment, the morphologies of the P-MnO_2 and Fe-MnO_2 appeared to be similar to that of E-MnO_2, as shown in Fig. 1e and i. This indicated that rich defects could be caused by plasma etching. Additionally, the porous structure of the nanosheets can lead to increased exposure of active sites as well as shortened charge transfer pathways, which is beneficial for the catalytic performance. With increasing plasma treating time, the edge surfaces of P-MnO_2-1~20 became increasingly porous, indicating the enhanced etching effect, as shown in Fig. S2. Additionally, for the optimal plasma treatment time, the increase in Fe species caused no obvious change in the nanosheet morphology (Fig. S3); this further proves that it is plasma etching rather than the Fe species that plays a key role in regulating the morphology. Next, we further investigated the samples *via* TEM and HRTEM. After decorating the P species *via* plasma treatment, Fig. 1f and g show that the P-MnO_2 maintained a rough porous nanosheet structure and had the MnO_2 phase. Furthermore, the energy-dispersive X-ray spectroscopy (EDS) results in Fig. 1h demonstrate uniform mapping of Mn, O, and P, confirming successful decoration of the P species. With decoration of the Fe species *via* plasma treatment, a rough porous nanosheet morphology and the phase of MnO_2 are indicated by the results shown in Fig. 1j and k. Additionally, the EDS results in Fig. 1l show a uniform distribution of Mn, O, and Fe, indicating successful decoration of the Fe species.

In order to identify the defect level, EPR investigation is performed. As shown in Fig. 2a, the signal at g = 2.003 indicates the existence of lattice distortions. Apparently, compared to pristine MnO_2, the signal of E-MnO_2, P-MnO_2 and Fe-MnO_2 is greatly strengthened, while no significant fluctuations in pristine MnO_2. The enhanced signals indicate the increase of lattice defects after plasma treatment and P/Fe decorated. The increased defective state of E-MnO_2 can be ascribed to oxide vacancies induced by plasma treatment. Further, the signals of P-MnO_2 and Fe-MnO_2 are stronger than that of E-MnO_2, which can be attributed to that the decorated P or Fe species caused the extra lattice distortions [25]. These lattice defects may bring more active sites, which are benefited for electrocatalytic process. To further explore the surface chemical states of the optimal samples, Fig. 2b and c show the XPS results of MnO_2. For pristine MnO_2, as shown in Fig. 2b, the peaks at 641.7 eV and 653.4 eV indicate the existence of Mn^{3+} while the peaks at 642.9 eV and 654.5 eV can be indexed to Mn^{4+} [26]. And the three characteristic peaks of 529.9 eV, 531.2 eV and 532.6 eV in O 1s spectra shown in Fig. 2c can be ascribed to the metal–oxygen bonds, OH^- groups and surface oxygen defects respectively [27]. After Ar plasma treatment, the proportion of Mn^{3+} dramatically increases than the Mn 2p spectra of E-MnO_2, as shown in Fig. S4b. The formation of more Mn^{3+} sites is correlated to the rich defects in E-MnO_2 [28], which can be attributed to the etching effect of plasma treatment. Besides, according to previous research [9], the Mn^{3+} sites could play an important role in promoting the catalytic performances of HER and OER. Specifically, the defective Mn^{3+} sites own a more ideal adsorption free energy for protons and H_2O molecules, as well as improve the conductivity of the MnO_2 with semiconductor properties. Thus, the HER would be greatly facilitated. Moreover, the OER can be promoted by rich Mn^{3+} since that the disproportionation reactions of Mn^{3+} to Mn^{2+} and Mn^{4+} benefit the evolution of O_2 [29,30]. After decorated the P species, the P 2p in Fig. 2d demonstrates that there are partial negatively charged P atoms greatly beneficial for the HER [14,15], which further confirms the successful decoration of the electroactive P species. Besides, as shown in Fig. 2e, the Mn 2p spectra of P-MnO_2 suggests that Mn^{3+} maintains a relatively high proportion. Additionally, as shown in Fig. 2f, the O 1s of P-MnO_2 suggests the obvious characteristic peak at 532.6 eV,

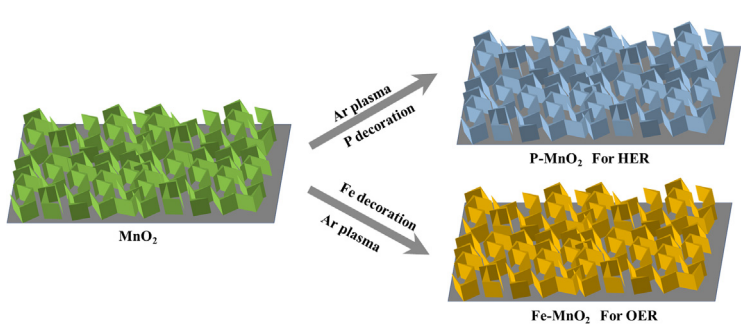

Scheme 1. Schematic illustration of fabrication of P-MnO_2 and Fe-MnO_2.

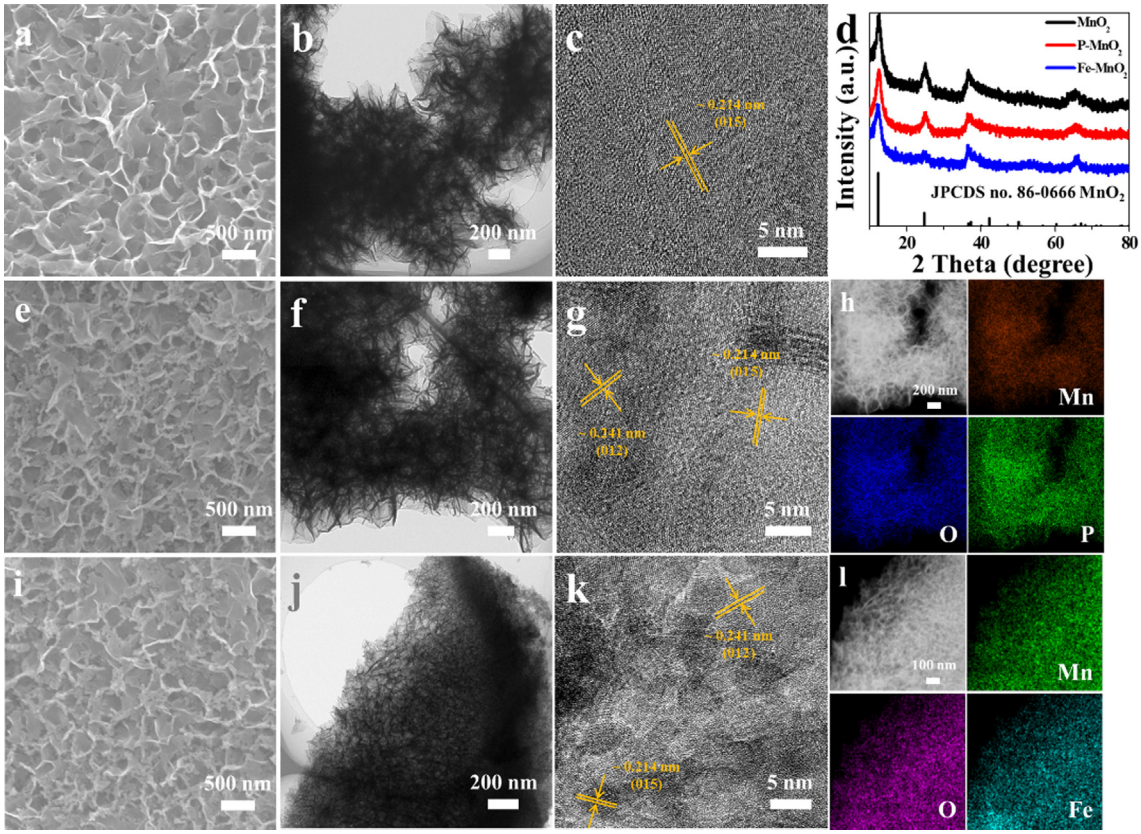

Fig. 1. (a) SEM image, (b) TEM image and (c) HRTEM image of MnO_2; (d) XRD patterns of the obtained samples; (e) SEM image, (f) TEM image, (g) HRTEM image and (h) corresponding element mapping of P-MnO_2; (i) SEM image, (j) TEM image, (k) HRTEM image and (l) corresponding element mapping of Fe-MnO_2.

indicating the existence of rich oxygen vacancies. While after decorated Fe species, the Fe 2p spectrum in Fig. 2g illustrates the coexistence of Fe^{2+} and Fe^{3+} [31], further confirming the successful decoration of Fe species on the surface of MnO_2. Further, as shown in Fig. 2h, the Mn 2p of Fe-MnO_2 demonstrates the existence of rich Mn^{3+}. Besides, the O 1s spectrum in Fig. 2i suggests the rich oxygen defects in Fe-MnO_2.

To determine the performance of the obtained surface activated MnO_2 for water splitting applications, related electrochemical tests were conducted with a three-electrode electrolyzer using 1 M KOH. For HER, the polarization curves of P-MnO_2-1~20 are shown in Fig. 3a, which demonstrate that the P-MnO_2-10 is the optimal sample. This shows that the plasma treatment time has an optimal range, which could be because excessive plasma treatment leads to mass loss of the electrocatalyst. Moreover, Fig. 3b shows the polarization curves of the Ni foam, MnO_2, E-MnO_2, P-MnO_2, and Pt/C. The P-MnO_2 has the best performance for HER among the samples in the control group with a low overpotential of 105 mV at 10 mA cm^{-2}. Compared with pristine MnO_2, the overpotential was reduced by 130 mV. Notably, this performance is quite competitive among recently reported electrocatalysts (Table S1). Additionally, E-MnO_2 performs better than pristine MnO_2, proving that oxygen defects induced by plasma etching are beneficial for HER catalytic activity. After decorating the P species via plasma treatment, realization of the lowest overpotential by P-MnO_2 confirmed the high electroactivity of the P species for the HER. To further explore the catalytic kinetic behavior, the Tafel slopes are plotted in Fig. 3c. P-MnO_2 had the smallest Tafel slope (69.3 mV dec^{-1}) among the Ni foam (160.6 mV dec^{-1}), MnO_2 (154.8 mV dec^{-1}), and E-MnO_2 (121.4 mV dec^{-1}), indicating a dramatically accelerated electron transfer process and favorable HER dynamics [6]. Additionally, the AC impedance spectra shown in Fig. 3d demonstrate that E-MnO_2 has a smaller radius than pristine MnO_2, indicating that the oxygen vacancies and defective Mn^{3+} sites could lead to a smaller charge transfer resistance. After decorating the P species, P-MnO_2 had the smallest radius among the curves of the investigated samples, which suggests accelerated adsorption of H_2O molecules and protons caused by the presence of the P species and oxygen vacancies. Notably, this is in agreement with the XPS analysis previously mentioned. Furthermore, to determine the density of active sites, the electrochemical active specific areas (ECSA) were estimated by the double layer capacitances (C_{dl}). The C_{dl} of E-MnO_2 is larger than that of pristine MnO_2, proving that oxygen defects induced by the plasma could lead to the exposure of more active sites. After decorating the P species, the C_{dl} of P-MnO_2 dramatically increased, suggesting that the decorated P species could serve as highly active sites for HER. To evaluate the stability of the as obtained P-MnO_2, chronopotentiometry was performed at 10 mA cm^{-2} (Fig. 3f); the steady curve demonstrates its good stability. Furthermore, the SEM images in Fig. S6a and S6b suggest that the nanosheet morphology was maintained after the long-duration HER test. Additionally, the XRD pattern of P-MnO_2 after the long-duration HER test corresponds well with δ-MnO_2 (JPCDS no. 86-0666), indicating there was no alteration in the phase. According to the above analysis, the excellent performance of P-MnO_2 can be attributed to the surface activated strategies with the decorated electroactive P species and rich vacancies, which can accelerate the absorption of protons, promote charge transfer, and provide more active sites.

The OER activities of the obtained samples are shown in Fig. 4. The polarization curves of Fe-MnO_2 with different amounts of Fe species decorated on the surface are shown in Fig. 4a. It can be seen

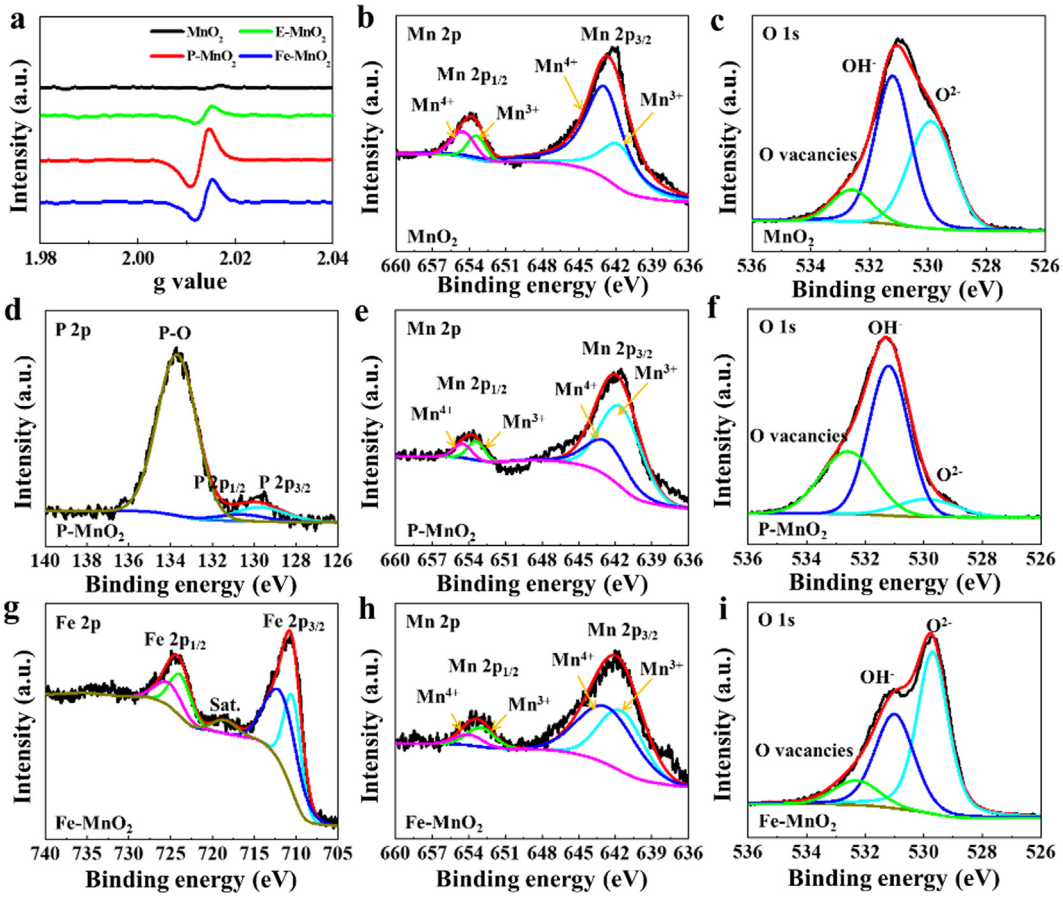

Fig. 2. (a) EPR spectra of MnO_2, E-MnO_2, P-MnO_2 and Fe-MnO_2; XPS spectra of (b) Mn 2p and (c) O 1s in MnO_2; XPS spectra of (d) P 2p, (e) Mn 2p and (f) O 1s in P-MnO_2; XPS spectra of (g) Fe 2p, (h) Mn 2p and (i) O 1s in Fe-MnO_2.

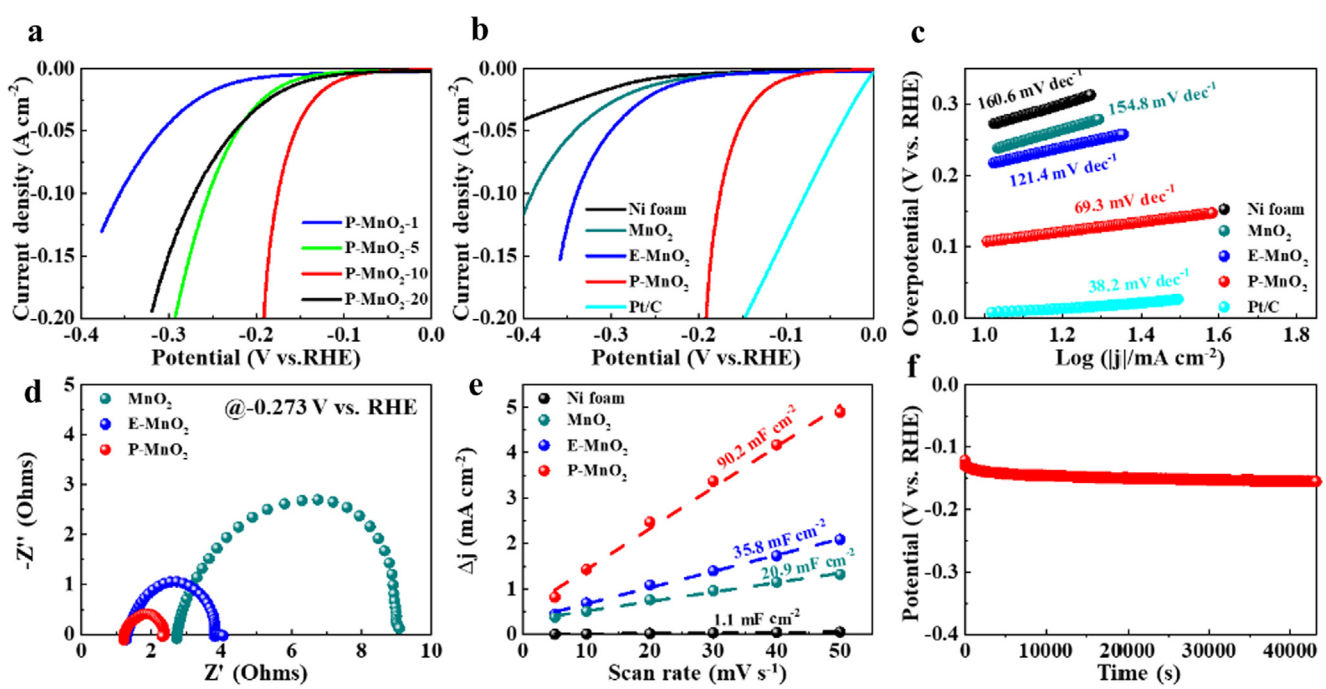

Fig. 3. (a) LSV curves of P-MnO_2-1, 5, 10, 20. (b) LSV curves, (c) corresponding Tafel plots, (d) Nyquist plots and (e) the estimated C_{dl} values of obtained catalysts for HER tests. (f) Chronopotentiometry measurements for P-MnO_2 (without iR correction).

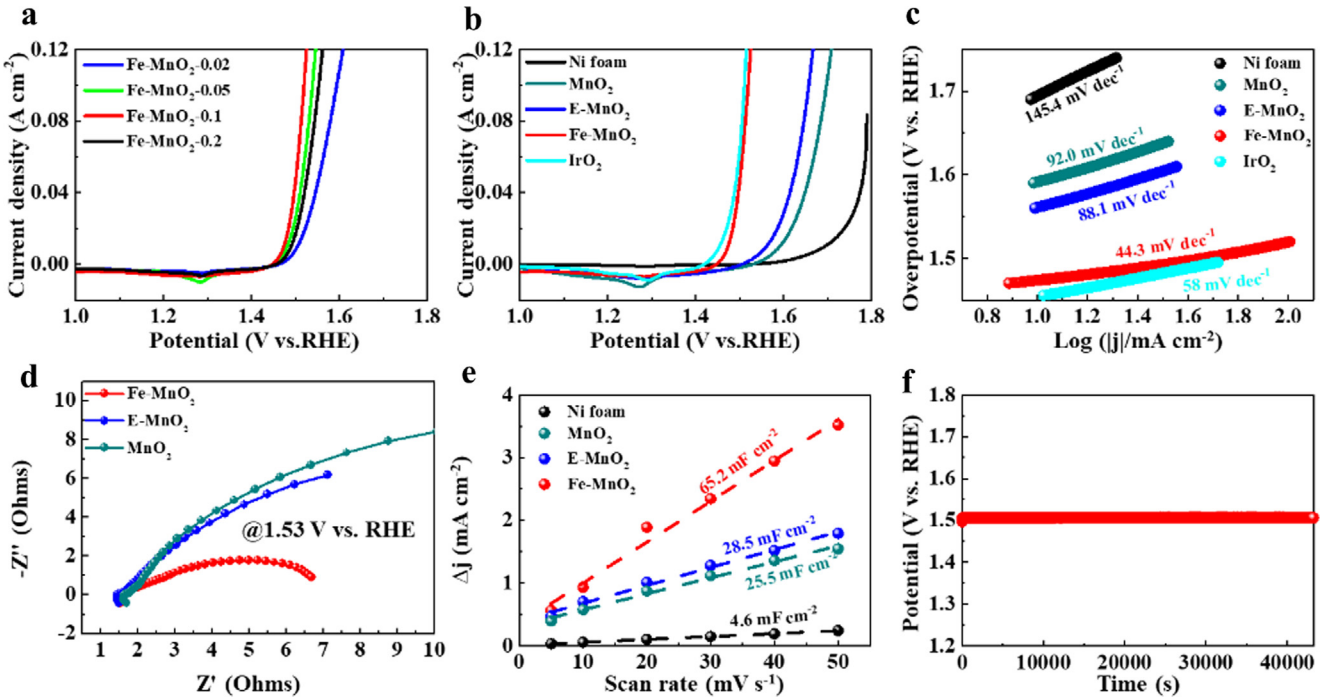

Fig. 4. (a) LSV curves of P-MnO$_2$-1, 5, 10, 20. (b) LSV curves, (c) corresponding Tafel plots, (d) Nyquist plots and (e) the estimated C_{dl} values of obtained catalysts for HER tests. (f) Chronopotentiometry measurements for P-MnO$_2$ (without iR correction).

that Fe-MnO$_2$-0.1 was the optimal sample, suggesting that an optimal range exists for the Fe content. The polarization curves of the Ni foam, MnO$_2$, E-MnO$_2$, Fe-MnO$_2$, and IrO$_2$ are shown in Fig. 4b. The Fe-MnO$_2$ had the best performance for the OER, only needing an overpotential of 244 mV at 10 mA cm^{-2}. Compared with pristine MnO$_2$, the overpotential was reduced by 116 mV. It should be noted that such performance is competitive relative to existing electrocatalysts (Table S2). Furthermore, the performance of E-MnO$_2$ was better than pristine MnO$_2$, proving that the oxygen defects induced by plasma etching were beneficial for OER catalytic activity. After decorating the Fe species via plasma treatment, the lowest overpotential for Fe-MnO$_2$ confirmed the high electroactivity of the Fe species towards OER. To further determine the kinetic behavior, the Tafel slopes are plotted in Fig. 4c. The Fe-MnO$_2$ had the smallest Tafel slope (44.3 mV dec^{-1}) among Ni foam (145.4 mV dec^{-1}), MnO$_2$ (92.0 mV dec^{-1}), E-MnO$_2$ (88.1 mV dec^{-1}), and even IrO$_2$ (58 mV dec^{-1}), indicating dramatically improved OER dynamics. Additionally, the electrochemical impedance spectra shown in Fig. 4d demonstrate that the E-MnO$_2$ has a smaller radius than pristine MnO$_2$, indicating that oxygen vacancies and defective Mn^{3+} could lead to a smaller charge transfer resistance. After decorating the Fe species, Fe-MnO$_2$ had the smallest radius of the curves among the investigated samples, which suggests it has the smallest charge transfer resistance due to the contributions of the Fe species and oxygen vacancies; this is in agreement with the XPS analysis previously mentioned. Furthermore, the ECSA were estimated via C_{dl} to determine the density of active sites (Fig. 4e). The C_{dl} of E-MnO$_2$ was larger than that of pristine MnO$_2$, proving that the oxygen defects induced by plasma could lead to the exposure of more active sites. After decorating the Fe species, the C_{dl} of Fe-MnO$_2$ dramatically increased, suggesting that the decorated Fe species could serve as highly active sites for OER. Additionally, chronopotentiometry was performed at 10 mA cm^{-2} (Fig. 4f) to determine the stability of the as obtained Fe-MnO$_2$. The steady curve demonstrates the good stability. Furthermore, no obvious change was found in the Fe-MnO$_2$ morphology after the long-duration OER test, as shown in Fig. S8a and S8b, further suggesting the good durability of Fe-MnO$_2$. The XRD pattern of Fe-MnO$_2$ after

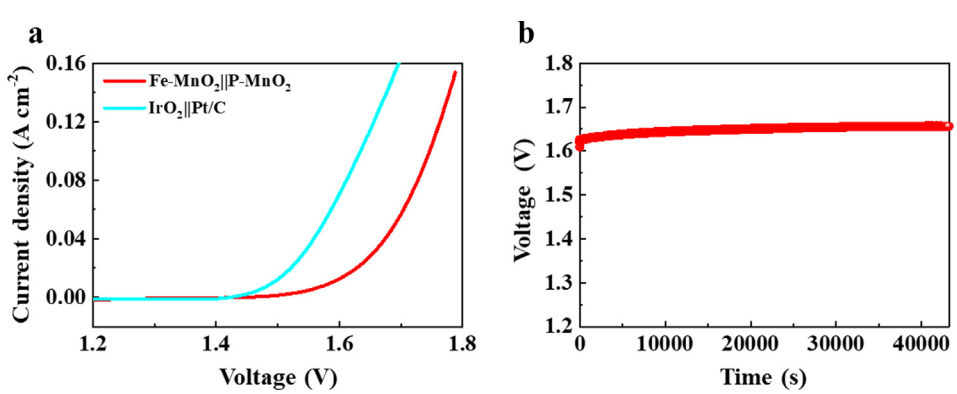

Fig. 5. Polarization curves of Fe-MnO$_2$||P-MnO$_2$ and IrO$_2$||Pt/C for overall water splitting. (b) Long-term stability for Fe-MnO$_2$||P-MnO$_2$ at 10 mA cm^{-2}.

these tests corresponded well with δ-MnO_2, indicating that there were no phase changes. Additionally, XPS tests were performed with the Fe-MnO_2 after the long-duration OER cycling tests. As shown in Fig. S9a, the Fe 2p spectra show the coexistence of Fe^{2+} and Fe^{3+}. Furthermore, the Mn 2p spectrum (Fig. S9b) indicates that the proportion of Mn^{3+} is still high, which could promote charge transfer. It should be noted that the ratio of OH^- is higher than that of the original sample (Fig. S9c), which could be attributed to the Fe species being beneficial for the absorption of OH^- [32]. Additionally, the decorated Fe species may be converted in situ to the corresponding oxide/hydroxide with higher OER activity [33]. In summary, the surface activation strategy with decorated Fe species and rich oxygen vacancies was beneficial for promoting the OER performance. This can be attributed to the accelerated catalytic process, enhanced charge transfer, and the increased number of active sites.

Encouraged by the good HER performances of P-MnO_2 and the satisfying OER performances of Fe-MnO_2, the overall water splitting is measured by using P-MnO_2 as cathode and Fe-MnO_2 as anode. As shown in Fig. 5a, the polarization curves of Fe-MnO_2||P-MnO_2 and IrO_2||Pt/C are measured by two-electrode water splitting device. Notably, the Fe-MnO_2||P-MnO_2 cell only needs 1.59 V to achieve 10 mA cm^{-2}, competitive among previous electrocatalysts in Table S3. Besides, the chronopotentiometry results of Fe-MnO_2||P-MnO_2 electrolyzer shown in Fig. 5b, and the steady curve demonstrates the good stability. Consequently, the surface activated MnO_2 electrodes could serve as promising candidates for overall water splitting.

4. Conclusion

Although previous works reported the MnO_2 based materials served as electrocatalysts, most of these catalysts only exhibited the catalytic performance of OER for water splitting [11–13]. There is a lack of researchs on MnO_2 based catalysts for HER, and it is expected to further improve its OER performance. Despite that the 2D MnO_2 based materials show unsatisfied HER and OER catalytic activity, but the 2D nanostructure materials possess promising potential to be applied as electrocatalysts due to their unique advantages. In our work, the activated MnO_2 nanosheets had been successfully constructed through a plasma engineering. The activated MnO_2 nanosheets provided numerous oxygen vacancies and exposed catalytic active sites that promote the catalytic process for water splitting. As for HER, the decorated P species and oxygen vacancies could promote the absorption of protons and increased the ratio of Mn^{3+}, and thus increasing the active sites exposure and accelerating electronic transfer. As for OER, the Fe sites and oxygen vacancies could promote the absorption of OH– and the formation of stable Mn^{3+}, which determined the catalytic reaction efficiency. Accordingly, P-MnO_2 and Fe-MnO_2 suggested remarkable catalytic performances towards HER and OER respectively, with low overpotentials of 105 mV at 10 mA cm^{-2} for HER and 244 mV at 10 mA cm^{-2} for OER. Further, the as constructed two electrodes water splitting device possessed low voltage of 1.59 V at 10 mA cm^{-2}. The performance of this catalyst surpasses most of the investigated MnO_2 based catalysts. The work emphasizes the application of surface activation of 2D materials in the development of advanced electrocatalysts for water splitting.

CRediT authorship contribution statement

Pengcheng Wang: Conceptualization, Methodology, Data curation, Software, Writing - original draft. **Yaotian Yan:** Investigation, Writing - review & editing. **Jian Cao:** Supervision. **Jicai Feng:** Formal analysis. **Junlei Qi:** Funding acquisition, Writing - review & editing.

Declaration of Competing Interest

The authors declare that they have no known competing financial interests or personal relationships that could have appeared to influence the work reported in this paper.

Acknowledgements

The support from the National Natural Science Foundation of China (Grant Nos 51575135, 51622503, U1537206, 21871066 and 51621091) and Natural Science Foundation of Heilongjiang Province of China (YQ2019E023) is highly appreciated. We would like to thank professor Weidong Fei for his valuable guidance on the energy conversion mechanism.

Appendix A. Supplementary material

Supplementary data to this article can be found online at https://doi.org/10.1016/j.jcis.2020.10.073.

References

[1] R. Zhang, J. Huang, G. Chen, W. Chen, C. Song, C. Li, K. Ostrikov, Plasma-heteroatom-doped Ni-V-Fe trimetallic phospho-nitride as high-performance bifunctional electrocatalyst, Appl. Catal. B: Environ. 245 (2019) 414.
[2] S. Park, Y. Shao, J. Liu, Y. Wang, Oxygen electrocatalysts for water electrolyzers and reversible fuel cells: status and perspective, Energy Environ. Sci. 5 (2012) 9331.
[3] Q. Liang, L. Zhong, C. Du, Y. Luo, J. Zhao, Y. Zheng, J. Xu, J. Ma, C. Liu, S. Li, Q. Yan, Interfacing epitaxial dinickel phosphide to 2D nickel thiophosphate nanosheets for boosting electrocatalytic water splitting, ACS Nano 13 (2019) 7975.
[4] Y. Gorlin, T. Jaramillo, A bifunctional nonprecious metal catalyst for oxygen reduction and water oxidation, J. Am. Chem. Soc. 132 (2010) 13612.
[5] Z. Wu, L. Huang, H. Liu, H. Wang, Element-specific restructuring of anion-and cation-substituted cobalt phosphide nanoparticles under electrochemical water-splitting conditions, ACS Catal. 9 (2019) 2956.
[6] S. Chu, W. Chen, G. Chen, J. Huang, R. Zhang, C. Song, X. Wang, C. Li, K. Ostrikov, Plasma-doping-enhanced overall water splitting: case study of NiCo hydroxide electrocatalyst, Appl. Catal. B: Environ. 243 (2019) 573.
[7] Y. Zhang, Y. Tan, H. Stormer, P. Kim, Experimental observation of the quantum Hall effect and Berry's phase in graphene, Nature 438 (2005) 201.
[8] A. Thenuwara, E. Cerkez, S. Shumlas, N. Attanayake, I. McKendry, L. Frazer, E. Borguet, Q. Kang, R. Remsing, M. Klein, Nickel confined in the interlayer region of birnessite: an active electrocatalyst for water oxidation, Angew. Chem., Int. Ed. 55 (2016) 10381.
[9] Y. Zhao, C. Chang, F. Teng, Y. Zhao, G. Chen, R. Shi, G. Waterhouse, W. Huang, T. Zhang, Defect-engineered ultrathin δ-MnO_2 nanosheet arrays as bifunctional electrodes for efficient overall water splitting, Adv. Energy Mater. 7 (2017) 1700005.
[10] G. Yan, Y. Lian, Y. Gu, C. Yang, H. Sun, Q. Mu, Q. Li, W. Zhu, X. Zheng, M. Chen, J. Zhu, Z. Deng, Y. Peng, Phase and morphology transformation of MnO_2 induced by ionic liquids toward efficient water oxidation, ACS Catal. 8 (2018) 10137.
[11] B. Kang, X. Jin, S. Oh, S. Patil, M. Kim, S. Kim, S. Hwang, An effective way to improve bifunctional electrocatalyst activity of manganese oxide via control of bond competition, Appl. Catal. B: Environ. 236 (2018) 107.
[12] Y. Zhao, J. Zhang, W. Wu, X. Guo, P. Xiong, H. Liu, G. Wang, Cobalt-doped MnO_2 ultrathin nanosheets with abundant oxygen vacancies supported on functionalized carbon nanofibers for efficient oxygen evolution, Nano Energy 54 (2018) 129.
[13] J. Kang, A. Hirata, L. Kang, X. Zhang, Y. Hou, L. Chen, C. Li, T. Fujita, K. Akagi, M. Chen, Enhanced supercapacitor performance of MnO_2 by atomic doping, Angew. Chem. 125 (2013) 1708.
[14] Y. Shi, B. Zhang, Recent advances in transition metal phosphide nanomaterials: synthesis and applications in hydrogen evolution reaction, Chem. Soc. Rev. 45 (2016) 1529.
[15] Q. Lv, J. Han, X. Tan, W. Wang, L. Cao, B. Dong, Featherlike NiCoP holey nanoarrys for efficient and stable seawater splitting, ACS Appl. Energy Mater. 2 (2019) 3910.
[16] D. Friebel, M. Louie, M. Bajdich, K. Sanwald, Y. Cai, A. Wise, M. Cheng, D. Sokaras, T. Weng, R. Alonso-Mori, R. Davis, J. Bargar, J. Nørskov, A. Nilsson, A. Bell, Identification of highly active Fe sites in (Ni, Fe) OOH for electrocatalytic water splitting, J. Am. Chem. Soc. 137 (2015) 1305.
[17] J. Teng, L. Shen, Y. Xu, T. Chen, X. Wu, Y. He, J. Chen, H. Lin, Effects of molecular weight distribution of soluble microbial products (SMPs) on membrane

fouling in a membrane bioreactor (MBR): Novel mechanistic insights, Chemosphere 248 (2020) 126013.
[18] M. Wu, Y. Chen, H. Lin, L. Zhao, L. Shen, R. Li, Y. Xu, H. Hong, Y. He, Membrane fouling caused by biological foams in a submerged membrane bioreactor: Mechanism insights, Water Res. 181 (2020) 115932.
[19] J. Teng, M. Wu, J. Chen, H. Lin, Y. He, Different fouling propensities of loosely and tightly bound extracellular polymeric substances (EPSs) and the related fouling mechanisms in a membrane bioreactor, Chemosphere 255 (2020) 126953.
[20] L. Rao, J. Tang, S. Hu, L. Shen, Y. Xu, R. Li, H. Lin, Inkjet printing assisted electroless Ni plating to fabricate nickel coated polypropylene membrane with improved performance, J. Colloid Interf. Sci. 565 (2020) 546–554.
[21] T. Sun, Y. Liu, L. Shen, Y. Xu, R. Li, L. Huang, H. Lin, Magnetic field assisted arrangement of photocatalytic TiO_2 particles on membrane surface to enhance membrane antifouling performance for water treatment, J. Colloid Interf. Sci. 570 (2020) 273–285.
[22] Y. Liu, L. Shen, H. Lin, W. Yu, Y. Xu, R. Li, T. Sun, Y. He, A novel strategy based on magnetic field assisted preparation of magnetic and photocatalytic membranes with improved performance, J. Membrane Sci. 612 (2020) 118378.
[23] L. An, J. Feng, Y. Zhang, R. Wang, H. Liu, G. Wang, F. Cheng, P. Xi, Epitaxial heterogeneous interfaces on N-$NiMoO_4$/NiS_2 nanowires/nanosheets to boost hydrogen and oxygen production for overall water splitting, Adv. Funct. Mater. 29 (2019) 1805298.
[24] Z. Zhang, X. Ma, J. Tang, Porous $NiMoO_{4-x}$/MoO_2 hybrids as highly effective electrocatalysts for the water splitting reaction, J. Mater. Chem. A 6 (2018) 12361.
[25] K. Zhang, G. Zhang, J. Qu, H. Liu, Disordering the atomic structure of Co(II) oxide via B-doping: an efficient oxygen vacancy introduction approach for high oxygen evolution reaction electrocatalysts, Small 14 (2018) 1802760.
[26] Y. Gu, Z. Lu, Z. Chang, J. Liu, X. Lei, Y. Li, X. Sun, Fe-doped Ni_3C nanodots in N-doped carbon nanosheets for efficient hydrogen-evolution and oxygen-evolution electrocatalysis, J. Mater. Chem. A 1 (2013) 10655.
[27] S. Lian, C. Sun, W. Xu, W. Huo, Y. Luo, K. Zhao, G. Yao, W. Xu, Y. Zhang, Z. Li, K. Yu, H. Zhao, H. Cheng, J. Zhang, L. Mai, Built-in oriented electric field facilitating durable $ZnMnO_2$ battery, Nano Energy 62 (2019) 79.
[28] K. Jin, H. Seo, T. Hayashi, M. Balamurugan, D. Jeong, Y.K. Go, J.S. Hong, K.H. Cho, H. Kakizaki, N. Bonnet-Mercier, M.G. Kim, S.H. Kim, R. Nakamura, K.T. Nam, Mechanistic investigation of water oxidation catalyzed by uniform, assembled MnO nanoparticles, J. Am. Chem. Soc. 139 (2017) 2277.
[29] T. Takashima, K. Hashimoto, R. Nakamura, Mechanisms of pH-dependent activity for water oxidation to molecular oxygen by MnO_2 electrocatalysts, J. Am. Chem. Soc. 134 (2012) 1519.
[30] D. Jeong, K. Jin, S.E. Jerng, H. Seo, D. Kim, S.H. Nahm, S.H. Kim, K.T. Nam, Mn_5O_8 nanoparticles as efficient water oxidation catalysts at neutral pH, ACS Catal. 5 (2015) 4624.
[31] Z. Liu, X. Wang, T. Ouyang, L. Wang, J. Zhong, T. Ma, Redox-Inert Fe^{3+} ions in octahedral sites of Co-Fe spinel oxides with enhanced oxygen catalytic activity for rechargeable Zinc-Air batteries, Angew. Chem. Int. Ed. 131 (2019) 13425.
[32] C. Peng, N. Ran, G. Wan, W. Zhao, Z. Kuang, Z. Lu, C. Sun, J. Liu, L. Wang, H. Chen, Engineering active Fe sites on nickel-iron layered double hydroxide through component segregation for oxygen evolution reaction, ChemSusChem 12 (2020) 811–818.
[33] E. Hu, J. Ning, D. Zhao, C. Xu, Y. Lin, Y. Zhong, Z. Zhang, Y. Wang, Y. Hu, A room-temperature postsynthetic ligand exchange strategy to construct mesoporous Fe-Doped CoP hollow triangle plate arrays for efficient electrocatalytic water splitting, Small 14 (2018) 1704233.